



Plasmonic effect of bimetallic TiO₂/Al₂O₃ nanoparticles in tellurite glass for surface-enhanced Raman scattering applications

Ixora Ferodolin^a, Asmahani Awang^{a,*}, S.K. Ghoshal^{b,**}, Alireza Samavati^c, Chee Fuei Pien^a, Jedol Dayou^d

^a Physics with Electronics Programme, Faculty of Science and Natural Resources, Universiti Malaysia Sabah, 88400, Kota Kinabalu, Sabah, Malaysia

^b Advanced Optical Materials Research Group, Physics Department & Laser Centre, Faculty of Science, Universiti Teknologi Malaysia, UTM, 81310, Johor Bahru, Johor, Malaysia

^c Physics Department, Faculty of Science, Universiti Teknologi Malaysia, UTM, 81310, Johor Bahru, Malaysia

^d Energy, Vibration and Sound Research Group (e-VIBS), Faculty of Science and Natural Resources, Universiti Malaysia Sabah, 88400, Kota Kinabalu, Sabah, Malaysia

ARTICLE INFO

Keywords:

SPR
Nanoparticles
SERS
Energy transfer
Anisotropic

ABSTRACT

Understanding the surface plasmon resonance (SPR) assisted spectroscopic properties of the glasses via the incorporation of the bimetallic nanoparticles (NPs) is a prerequisite for the surface-enhanced Raman scattering (SERS) applications. The texture, structures, and optical traits of melt-quenched synthesized Er³⁺-doped tellurite glasses were modified by incorporating bimetallic TiO₂/Al₂O₃ NPs. The as-quenched samples were characterized using diverse techniques, where the X-ray diffraction (XRD) analyses confirmed their amorphous nature. The surface roughness of the glass was improved from 6.1 nm (TZNETi glass) to 9.3 nm (TZNETiAl_{0.6} glass). The SPR bands of the bimetallic TiO₂/Al₂O₃ NPs were probed at 554 nm and 827 nm. The photoluminescence (PL) intensity enhancement was evidenced due to the NPs SPR-mediated strong local field effect and energy transfer between the metallic NPs and Er³⁺ ions. The amplification in the Raman intensity due to the NPs SPR-mediated enhanced electromagnetic field contribution. The proposed glass system may be beneficial as substrate for the SERS applications.

1. Introduction

Plasmonics is a new paradigm that governs the exploitation of the metallic nanostructures and light. The customization of the dimension, shape, composition, and features of the two and three dimensional plasmonic structures paves the way for achieving novel emergent properties [1]. Enlargement of the electromagnetic fields associated with the plasmon resonances of the nanostructures generates strong local optical fields favorable for the surface-enhanced Raman scattering (SERS) applications [2]. Presently, positioning of the molecules in the close vicinity of a rough noble-metal surface has widely been investigated to substantially enhance the Raman signal for exploring the potential of SERS performance [3].

In fact, electrochemically-roughened metal electrodes emerged as the earliest method to produce the original substrates for the SERS uses [4]. Meanwhile, the formation of the metal particle layers on suitable substrates such as quartz or glass has been explored to produce the SERS

substrate for molecular detection applications [5]. Various techniques have been developed to produce SERS substrate, including the electron-beam lithography, focused ion-beam milling, evaporation or pulsed laser deposition (PLD) of metallic NPs, roughened metal electrodes, acid-etching of metal foil, iodination of evaporated silver foil, replication method of polymer surfaces, nanospheres lithography, step-by-step assembly of nanoparticles (NPs) multilayers, and metal nanoshells [6–10]. Nevertheless, the metal NPs emerged as the most favorable materials due to their significant enhancement, easy preparation, and beneficial features of absorbing species in terms of the optimal surface area [11].

Diverse experimental efforts have been made to produce novel NPs with various geometries to support the well-defined plasmon resonances with controlled frequencies. The unique near-field features such as the plasmon resonant frequency, near-field amplitude spatial distribution of nanostructure surface, orientations affecting the polarization of the incident light wave, and spatial extent of the near field were exhibited

* Corresponding author.

** Corresponding author.

E-mail addresses: asmahani_awang@ums.edu.my (A. Awang), sibkrishna@utm.my (S.K. Ghoshal).

<https://doi.org/10.1016/j.jlumin.2021.118488>

Received 1 February 2021; Received in revised form 22 July 2021; Accepted 17 September 2021

Available online 23 September 2021

0022-2313/© 2021 Elsevier B.V. All rights reserved.

Table 1
Glass compositions (mol%).

Glass code	TeO ₂	ZnO	Na ₂ O	Er ₂ O ₃	TiO ₂	Al ₂ O ₃
TZNE	70.0	20	9	1	0	0
TZNETi	69.7	20	9	1	0.3	0
TZNETiAl0.1	69.6	20	9	1	0.3	0.1
TZNETiAl0.2	69.5	20	9	1	0.3	0.2
TZNETiAl0.3	69.4	20	9	1	0.3	0.3
TZNETiAl0.4	69.3	20	9	1	0.3	0.4
TZNETiAl0.5	69.2	20	9	1	0.3	0.5
TZNETiAl0.6	69.1	20	9	1	0.3	0.6
TZN	70.0	20	9	0	0	0
TZNTi	69.7	20	9	0	0.3	0
TZNTiAl0.1	69.6	20	9	0	0.3	0.1
TZNTiAl0.2	69.5	20	9	0	0.3	0.2
TZNTiAl0.3	69.4	20	9	0	0.3	0.3
TZNTiAl0.4	69.3	20	9	0	0.3	0.4
TZNTiAl0.5	69.2	20	9	0	0.3	0.5
TZNTiAl0.6	69.1	20	9	0	0.3	0.6

by these nanostructured geometries [2]. An all-inclusive detail of the molecular fingerprint can be accomplished by implementing the sensitivities of the single-molecule level via the SERS method. This method employs the intensification in the Raman intensity under certain circumstances in which the molecules are located and surrounded by the metallic nanostructures [1]. Several studies have been carried out to produce SERS substrates such as the monometallic NPs prior to the noble metals such as gold (Au) and silver (Ag). The exploitation of the

bimetallic NPs in combination with different types of metals stimulates the SERS activity in glass substrates remains deficient. Thus, it is prerequisite to explore and understand the vital interaction between the bimetallic NPs and the constituent atoms in the glass matrix to generate the SERS activity [5,12].

Undoubtedly, SERS is a powerful technique that provides a wide-ranging structural interpretation. However, slight changes in the orientation and structure of the molecules lead to considerable effect due to the sensitivities of SERS [13]. In addition, deviations on the optical properties from those of idealized NPs might occur due to the size inaccuracies and nanoscale surface roughness inherited practically for most of the fabricated metallic NPs [14]. Tuning the growth of NPs onto the selected areas of the substrate facilitates the feasibility of using SERS in miniaturized technologies or accessible integration into the industrial processes [12]. To the best of our knowledge, the nucleation of the TiO₂/Al₂O₃ NPs in the interior part of the glass has not been reported. Most of the reports existing in the literature are dealt with the growth of the TiO₂/Al₂O₃ NPs in the exterior part of the glass, deposited on the glass surface as the thin film or as filler for the glass ionomer cements [15–20]. Nevertheless, an in-depth insight governing the correlation between the bimetallic nanostructures and constituent atoms in the glass matrix is required for better understanding of the spectroscopic properties of the glass.

Metal oxide NPs are integral parts of diverse applications such as catalysts, sensors, semiconductors, medical science, capacitors, and batteries [21]. Al₂O₃ offers beneficial features such as high thermal



Fig. 1. Glass samples without Er³⁺.

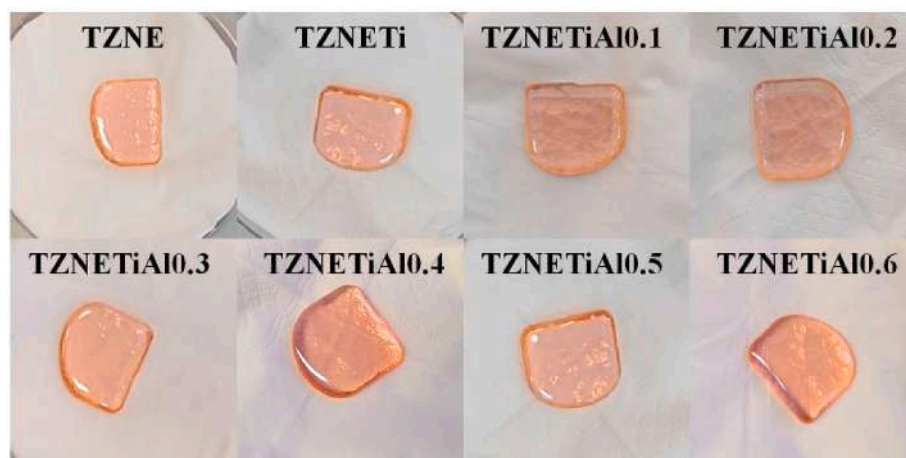


Fig. 2. Glass samples containing Er³⁺.

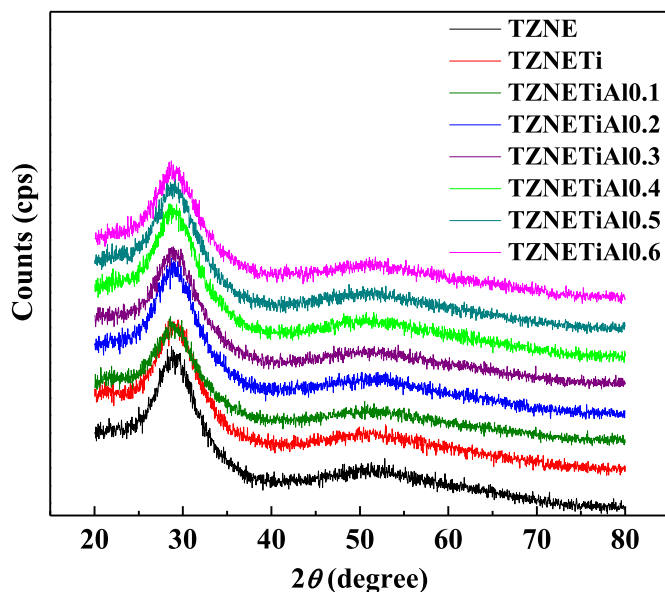


Fig. 3. XRD pattern of the glasses with varying concentration of NPs.

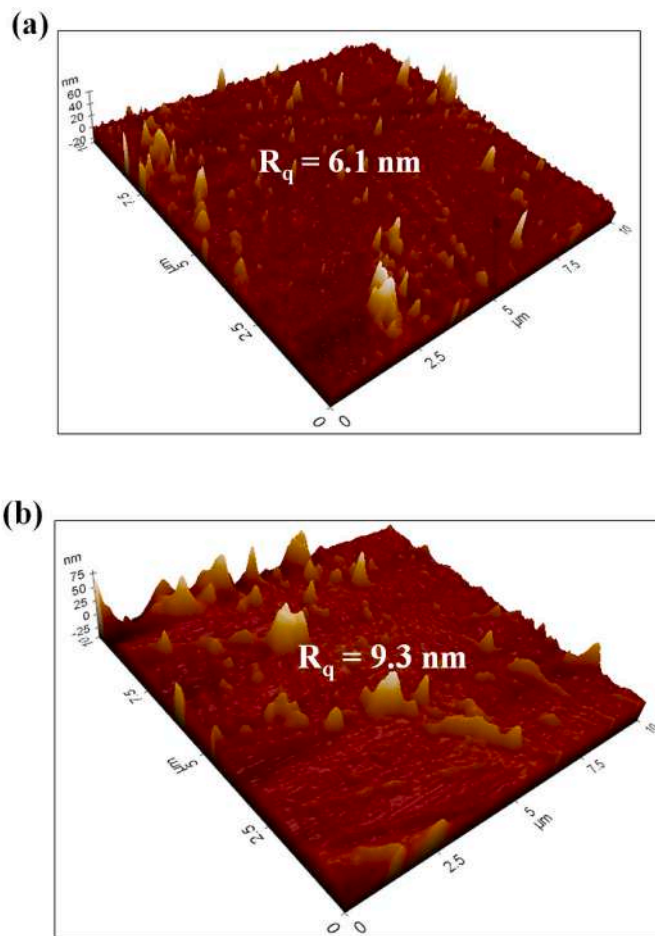


Fig. 4. AFM surface topography of (a) TZNETi glass and (b) TZNETiAl0.6 glass.

stability and excellent mechanical strength, and also facilitates the formation of catalytic sites [22]. Meanwhile, TiO_2 is a very promising metal oxide semi-conducting material for photo-conversion applications such as photocatalytic reactions and is used as transport material in

photovoltaic cells prior to dye-sensitized solar cells (DSSC) and perovskite solar cells due to high quantum yield and a suitable electronic band structure [23]. It has been known that rare earth ions such as erbium ions possess extraordinary properties due to the optical transitions in the intra-4f shell and have a privilege as a popular dopant in various glass systems [24]. The energy states of rare earth ions are altered by local electric fields that generate Stark-splitting and dynamical perturbation such as thermal or homogeneous broadening in a glass or crystal host. The incorporation of bimetallic NPs to the glass containing rare earth ions leads to prominent effects and can be altered to achieve desired properties [25].

In the present research, based on the aforementioned facts, the bimetallic $\text{TiO}_2/\text{Al}_2\text{O}_3$ NPs were directly embedded in the interior part of the glass to achieve good SERS substrate. The concentration of the NPs was varied from 0.1 to 0.6 mol% to determine its impacts on the spectroscopic properties of the Er^{3+} -doped tellurite glasses produced using the standard melt-quenching technique. The surface topography, structure, and optical characteristics of these glasses were analyzed thoroughly. In addition, the Raman measurements were performed to evaluate the potential of the proposed glass composition as suitable substrate for the possible SERS applications.

2. Materials and methods

2.1. Preparation of glass samples

Series of glasses with composition of $(70-x-y)\text{TeO}_2-20\text{ZnO}-9\text{Na}_2\text{O}-1\text{Er}_2\text{O}_3-(x)\text{TiO}_2-(y)\text{Al}_2\text{O}_3$ where $x = 0.0$ and 0.3 mol%; $y = 0.0, 0.1, 0.2, 0.3, 0.4, 0.5$ and 0.6 mol% were prepared using the melt-quenching technique. The doping levels of Er^{3+} were kept low in order to avoid concentration quenching. Raw materials of TeO_2 (analytical grade purity 99%) from Acros, and ZnO (analytical grade purity 99%), Na_2O (analytical grade purity 80%), Er_2O_3 (analytical grade purity 99.9%), TiO_2 (analytical grade purity 99.5%), and Al_2O_3 (analytical grade purity 99.8%) from Sigma Aldrich were mixed thoroughly to attain a homogeneous powder mixture. A platinum crucible containing the powder of raw materials was placed in a furnace at 950°C for 20 min, and the melt was transferred into a brass mould after the complete melting process was done. The mould containing molten was subjected to cooling down process under room temperature for two days to remove thermal and mechanical strains of the glass. Thickness of glass samples were measured by using digital vernier caliper. All glass samples were with a thickness of approximately 3.43 mm. The details of glass code and glass composition are tabulated in Table 1.

2.2. Characterizations of glass samples

The amorphous nature of the as-quenched samples were examined using a PANalytical X'Pert 3 MRD with $\text{Cu-K}\alpha$ radiations ($\lambda = 1.54 \text{ \AA}$) operating at 40 kV and 30 mA, with a scanning angle (2θ) ranging from 20° to 80° . The absorption spectra in the range of 375–1100 nm were recorded using an Agilent Cary 60 spectrophotometer. The transmission electron microscopy (TEM, Thermo Fisher Scientific TALOS L120C) was used to take the image of the NPs inside the glass. The surface topography and surface roughness of the glass samples were analyzed using the Park Systems NX10 atomic force microscopy (AFM) with scan size of $10 \mu\text{m}$. The PL excitation and emission spectra were obtained (excited at 527 nm) via an Agilent Technologies Cary Eclipse Fluorescence Spectrophotometer. The excitation spectra were recorded at the emission wavelength of 550 nm. The Raman measurement in the range of $190\text{--}800 \text{ cm}^{-1}$ was performed on a Thermo Fisher DXR2xi spectrophotometer with excitation wavelength of 785 nm.

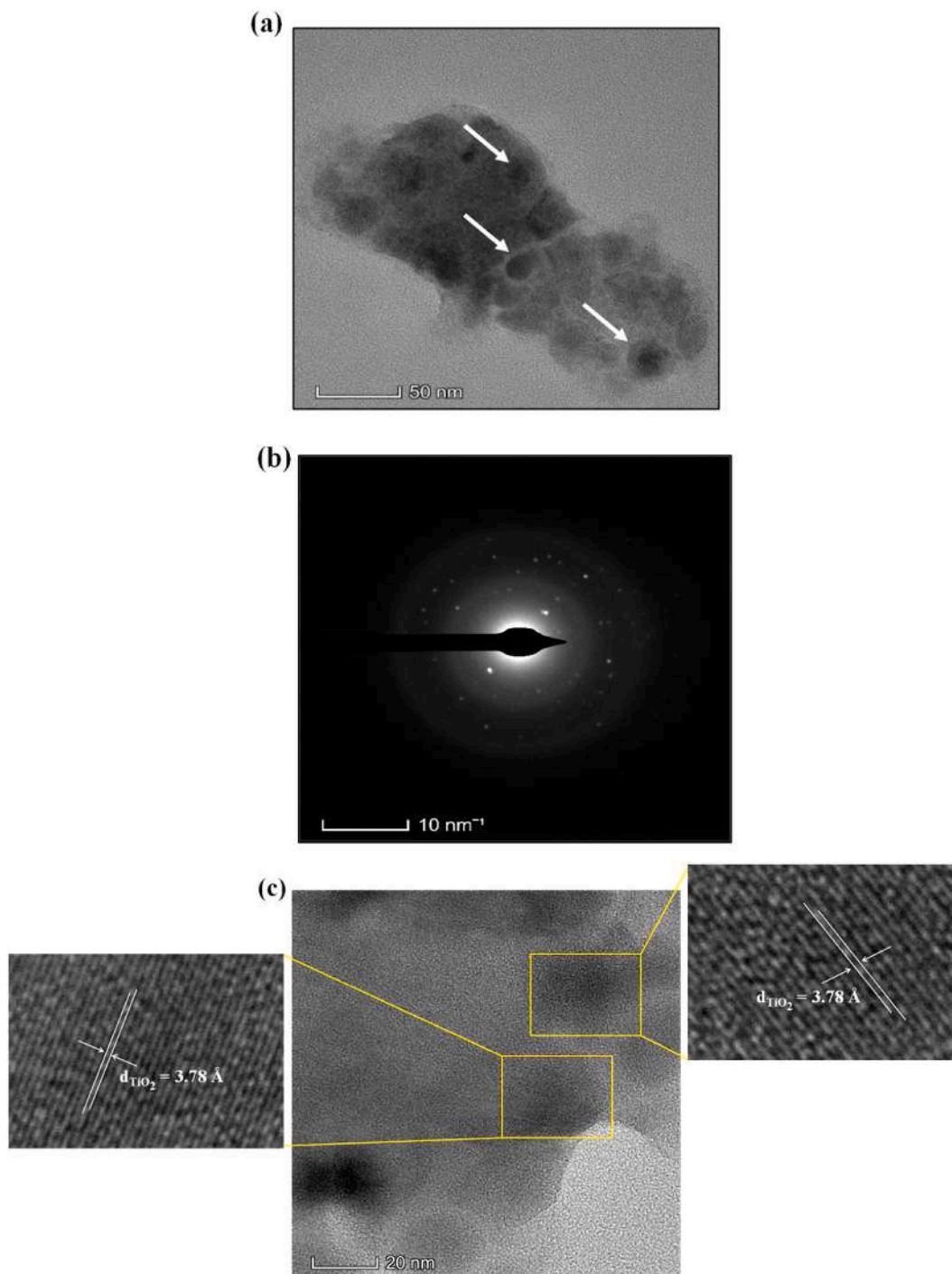


Fig. 5. (a) TEM image of TZNETi glass (b) Electron diffraction of TZNETi glass (c) Lattice fringe pattern of TZNETi glass. Inset shows magnification in the selected area.

3. Results and discussion

3.1. Physical and structural features

Fig. 1 shows the physical appearance of the glass samples (yellowish in color) without Er^{3+} doping (coded as TZN, TZNTi, TZNTiAl0.1, TZNTiAl0.2, TZNTiAl0.3, TZNTiAl0.4, TZNTiAl0.5, and TZNTiAl0.6 depending on the $\text{TiO}_2/\text{Al}_2\text{O}_3$ NPs contents). Fig. 2 illustrates the physical appearance of the glass samples (orangish in color) with Er^{3+} doping (coded as TZNE, TZNETi, TZNETiAl0.1, TZNETiAl0.2, TZNETiAl0.3, TZNETiAl0.4, TZNETiAl0.5, and TZNETiAl0.6 depending on

the Er^{3+} and $\text{TiO}_2/\text{Al}_2\text{O}_3$ NPs contents). In the host glass material, the occurrence of rare earth sites favors the absorption of distinct wavelengths in the visible spectrum, which leads to significant changes of glass color from pale yellow to orange [26]. However, the addition of TiO_2 and Al_2O_3 contents into the glass composition illustrated no color variation to the glass samples.

Fig. 3 exemplifies the XRD spectra of glass with varying TiO_2 and Al_2O_3 contents. The appearance of broad diffuse scattering located at $25\text{--}35^\circ$ with the absence of sharp crystallization peaks signifies the amorphous nature [27,28] and indicates the short range order of atoms in the glass [29,30].

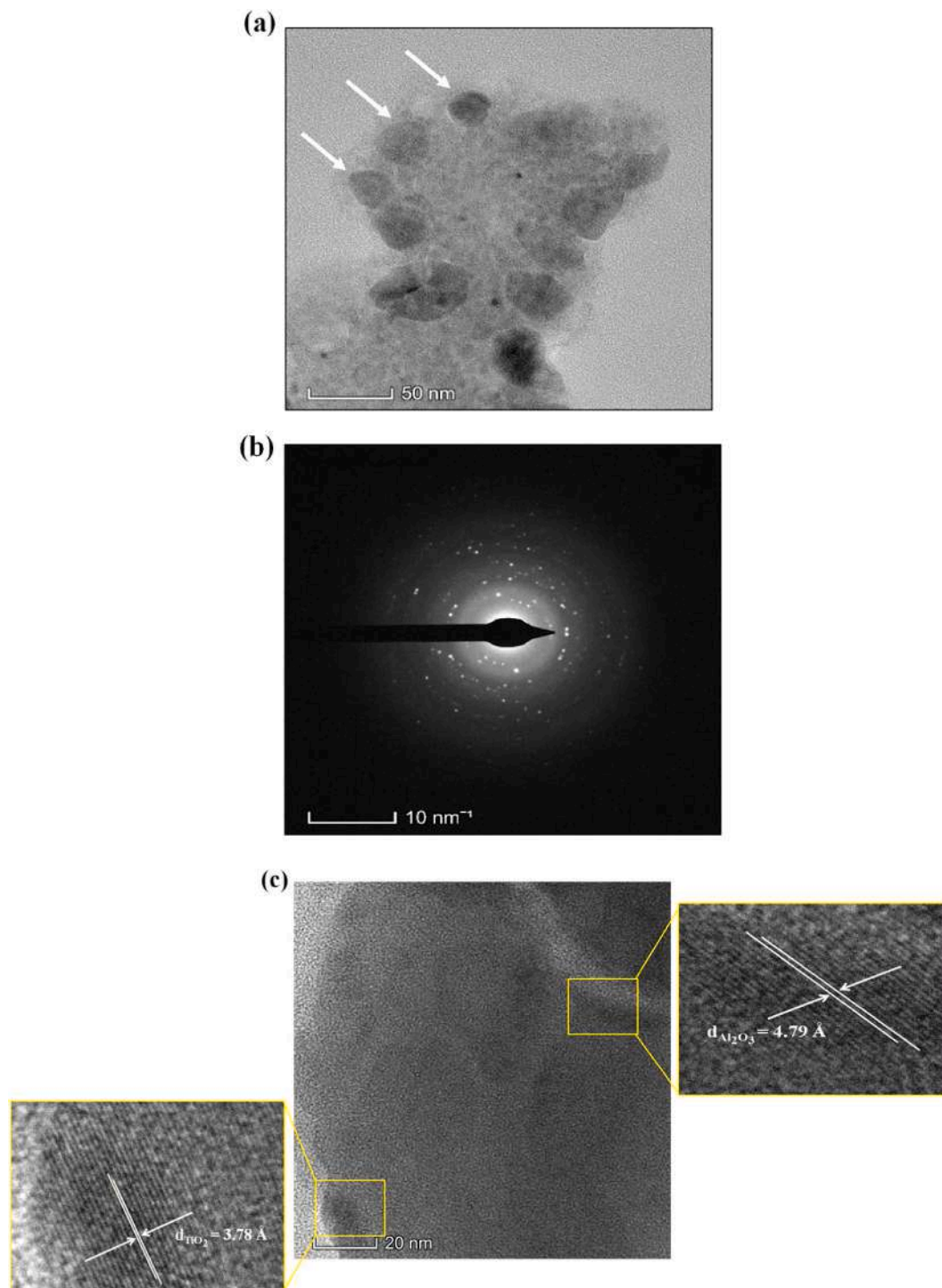


Fig. 6. (a) TEM image of TZNETiAl_{0.3} glass (b) Electron diffraction of TZNETiAl_{0.3} glass (c) Lattice fringe pattern of TZNETiAl_{0.3} glass. Inset shows magnification in the selected area.

3.2. Surface topography and morphology of nanoparticles

Fig. 4a and b shows the three-dimensional AFM images of the TZNETi and TZNETiAl_{0.6} samples, respectively, which revealed the difference in the surface topography due to the addition of monometallic and bimetallic NPs. The surface roughness was determined to verify the texture modification. The AFM image of TZNETi glass (Fig. 4a) shows the appearance of individually-scattered islands due to monometallic TiO₂ NPs. Meanwhile, the AFM image of TZNETiAl_{0.6} glass (Fig. 4b) illustrates the formation of some large and widely-scattered islands due

to the nucleation of the bimetallic TiO₂ and Al₂O₃ NPs. The appearance of large and wide scattered islands in the TZNETiAl_{0.6} glass signified the growth of the bimetallic NPs due to coalescence process [31]. The root mean squared average (R_q) roughness values of the TZNETi and TZNETiAl_{0.6} glass were found to increase from 6.1 nm to 9.3 nm, where the incorporation of high Al₂O₃ content signifies the growth of NPs. According to Okeil and Schneider [3], increasing the surface roughness is vital to enhancing the SERS performance due to the occurrence of potential hot spots. The generation of hot spots with sub-10 nm gaps provides a platform for the magnification of electromagnetic due to

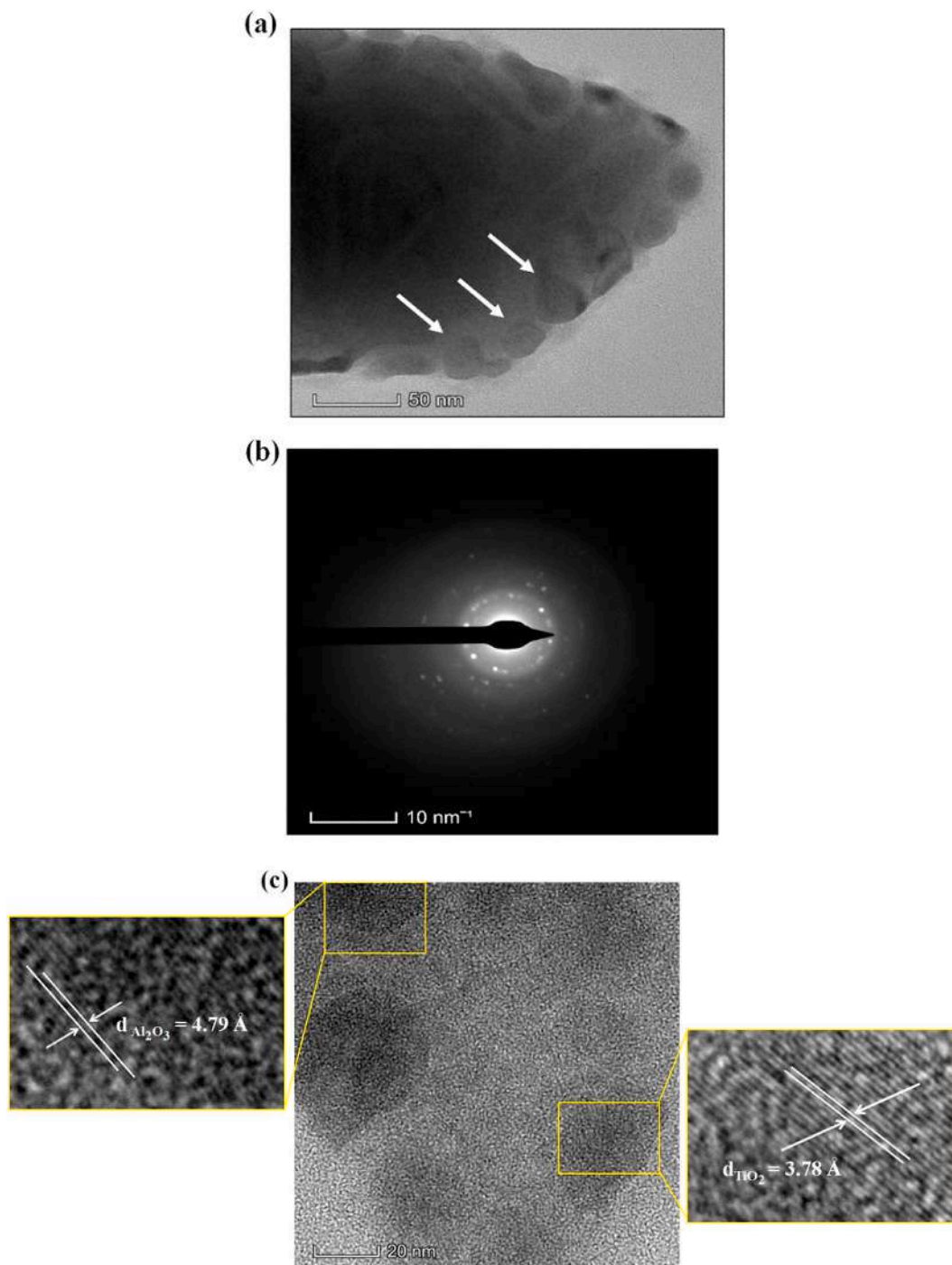


Fig. 7. (a) TEM image of TZNETiAl_{0.6} glass (b) Electron diffraction of TZNETiAl_{0.6} glass (c) Lattice fringe pattern of TZNETiAl_{0.6} glass. Inset shows magnification in the selected area.

constructive interference of plasmon resonance.

Fig. 5a represents the TEM image of the TZNETi glass containing monometallic TiO₂ NPs with non-spherical shape. Meanwhile, Figs. 6a and 7a show the TEM image of TZNETiAl_{0.3} and TZNETiAl_{0.6} glass containing bimetallic TiO₂ and Al₂O₃ NPs, respectively, reflecting the appearance of the NPs with elongated anisotropic shape [32]. These anisotropic NPs were different from the regular spheres (symmetrical) usually shown by the noble metals. The growth of NPs was stimulated by a thermodynamically-controlled or kinetically-controlled regime. In our case, the kinetically-controlled regime became dominant and led to the anisotropic growth of NPs with various shapes. Anisotropic growth at different facets, which was favored during the growth of crystal and

deviated from the thermodynamic equilibrium, causes infinitesimal modifications in reaction conditions. Subsequently, alteration in the surface-free energies at different facets became prominent [33]. It was found that the size of NPs in the longitudinal and transverse axes lies in the range of 15–34 nm and 11–20 nm for TZNETi glass. In contrast, the size of NPs in the longitudinal and transverse axes was respectively ranged from 26 to 39 nm and 19–35 nm for the TZNETiAl_{0.3} glass. Meanwhile, the size of NPs in the longitudinal and transverse axes of the TZNETiAl_{0.6} glass was respectively ranged from 25 to 48 nm and 19–32 nm. The size of the NPs was increased with further addition of NPs into TZNETiAl_{0.3} glass and TZNETiAl_{0.6} glass. Both manifested the NPs growth prior to the coalescence process triggered by the close proximity

Table 2

Size of NPs in the longitudinal and transverse axis and determination of aspect ratio in TZNETi, TZNETiAl0.3, and TZNETiAl0.6 glass.

TZNETi			TZNETiAl0.3			TZNETiAl0.6					
No.	Size of NPs		Aspect ratio, R	No.	Size of NPs		Aspect ratio, R	No.	Size of NPs		Aspect ratio, R
	Longitudinal, L (nm)	Transverse, D (nm)			Longitudinal, L (nm)	Transverse, D (nm)			Longitudinal, L (nm)	Transverse, D (nm)	
1	29	16	1.81	1	26	24	1.08	1	32	22	1.45
2	18	13	1.38	2	32	31	1.03	2	25	23	1.09
3	20	19	1.05	3	26	25	1.04	3	33	30	1.10
4	23	12	1.92	4	33	29	1.14	4	32	22	1.45
5	25	14	1.79	5	38	34	1.12	5	29	25	1.16
6	34	20	1.70	6	37	30	1.23	6	38	29	1.31
7	21	13	1.62	7	31	27	1.15	7	27	24	1.13
8	15	11	1.36	8	39	35	1.11	8	30	19	1.58
9	24	19	1.26	9	39	19	2.05	9	45	30	1.50
10	16	15	1.07	10	36	35	1.03	10	48	32	1.50

of the particles [32]. The aspect ratio of NPs defined as $R = L/D$, where L is the diameter of NPs on the longitudinal axis (major axis) and D is the diameter of NPs on the transverse axis (minor axis) [32,34] was found in the range of 1.05–1.92, 1.03–2.05, and 1.09–1.58 for the TZNETi glass, TZNETiAl0.3 glass, and TZNETiAl0.6 glass, respectively. It was observed that NPs exhibited a different value of the aspect ratio.

Figs. 5b, 6b and 7b illustrate the selected area electron diffraction (SAED) pattern with distribution of bright spots, which affirmed the distribution of NPs in the TZNETi glass, TZNETiAl0.3 glass, and TZNETiAl0.6 glass, respectively. The image taken from one of these areas indicated the existence of a polycrystalline structure component of NPs. Fig. 5c displays the lattice spacing of the monometallic NPs in the TZNETi glass. The inset showed the magnification in the selected area representing the lattice spacing of 3.78 Å corresponding to the TiO₂ NPs [35,36]. Figs. 6c and 7c show the lattice spacing of the bimetallic NPs in the TZNETiAl0.3 and TZNETiAl0.6 glass, respectively. The inset showed the magnification in the selected area of both glass samples, illustrating the lattice spacing of 3.78 Å and 4.79 Å corresponding to TiO₂ and Al₂O₃ NPs, respectively [37]. The occurrence of the lattice fringe due to the superimpose process of the zone axis orientation in a distinctive area of darkening reflected the diffraction and mass absorption of metallic NPs, which was distinguishable from the surrounding glass matrix [38]. The variations in the size of NPs along the longitudinal and transverse axes with specific values of aspect ratio are summarized in Table 2.

3.3. Surface plasmon resonance and surface-enhanced Raman scattering

Fig. 8a depicts the absorption spectra of the glasses, which comprised of eight absorption bands positioned at 409 nm, 450 nm, 491 nm, 523 nm, 544 nm, 653 nm, 799 nm, and 975 nm due to the transition from the ground state (⁴I_{15/2}) of Er³⁺ to the excited states of ²H_{9/2}, ⁴F_{3/2}, ⁴F_{7/2}, ²H_{11/2}, ⁴S_{3/2}, ⁴F_{9/2}, ⁴I_{9/2}, and ⁴I_{11/2}, respectively. Nevertheless, the Ti and Al plasmon bands were not observed in the glass containing the metallic NPs and Er³⁺ ions due to the intervention/dominance of the Er³⁺ peaks to the visibility of the plasmon band. The absorption spectra of the Er³⁺ in the visible region surpassed the plasmon band intensity of the metallic NPs [39]. Therefore, the other samples containing the same amount of metallic NPs without erbium were prepared to investigate the positions of the plasmon bands in the glass.

Fig. 8b and c illustrate a clear evidence of the SPR absorption bands positioned at 554 nm and 827 nm corresponding to the Ti and Al atoms, respectively. The glass containing monometallic TiO₂ NPs (TZNETi glass) showed the appearance of one plasmon band at 554 nm. Meanwhile, the glass containing both TiO₂ and Al₂O₃ bimetallic NPs (TZNETiAl0.1, TZNETiAl0.2, TZNETiAl0.3, TZNETiAl0.4, TZNETiAl0.5, and TZNETiAl0.6 glass) revealed two plasmon bands positioned at 554 nm and 827 nm. According to Naidoo and Ismaila [40], the optical spectra of uniformly-distributed particles depict a strong and prominent SPR peak. However, in this study, the SPR of broadening bands with less intensity

was observed, reflecting the distribution of the NPs with inconsistent symmetry.

The optical band gaps of the glass samples were calculated using the following equation [41,42]:

$$\alpha(\omega) = \frac{\beta(\hbar\omega - E_{opt})^n}{\hbar\omega} \quad (1)$$

where β is a constant, E_{opt} is the optical band gap, $\alpha(\omega)$ is the absorption coefficient at an angular frequency of $\omega = 2\pi\nu$, h is the Planck constant divided by 2π , and n is the index that exhibits the values of 0.5, 1.5, 2, and 3 depending on the nature of electronic transitions responsible for the absorption. Meanwhile, the extent of the exponential tail of the absorption edge in Urbach energy can be expressed as [43]:

$$\alpha(\omega) = \beta \exp\left(\frac{\hbar\omega}{E_{tail}}\right) \quad (2)$$

where E_{tail} is the width of band tails of electron states.

Fig. 9a and b shows the Tauc plot for direct band gap and indirect band gap, while Fig. 9c displays the absorption coefficient dependence of the photon energy. The direct band gap, indirect band gap, and Urbach energy were varied in the range of 3.146–3.165 eV, 2.920–3.104 eV, and 0.232–0.428 eV, respectively. The introduction of the TiO₂ NPs in glass matrix (TZNETi glass) caused a decrease in both direct and indirect band gap energies. The doping of TiO₂ with rare earth metal (Er₂O₃) extended the recombination time of the charge carriers and subsequently enhanced their separation efficiency. The generated multi-electrons configuration acted as a shallow trap for the photo-generated electrons and holes, which was attained due to the 4f electrons in the rare earth elements [44]. In addition, the inclusion of the small amounts of Al₂O₃ content (0.1 mol%) in the glass matrix (TZNETiAl0.1 glass) was enabled to increase both direct and indirect band gap energy due to generation of the additional carries from the donor Al atoms. This, in turn, led to the movement of the Fermi level approaching conduction band, hence increasing the band gap [45].

Further addition of the Al₂O₃ (from 0.2 to 0.6 mol%) showed a gradual decrease in the direct band gap and indirect band gap energies. This can be explained by correlating the decrement of band gap with the growth of NPs. Al₂O₃ NPs initiates the collective effect and subsequently ignites a massive cluster shifting or size increase on the sp² cluster due to the position of metal particles on the both ends of the energy gap that connected to the sp² sites. The ends of the energy gap consist of the occupied π and unoccupied π^* states. Thus, a distortion occurred in the Fermi energy level (reduction in size), and the effective optical band gap of glass reduced [40]. Meanwhile, the attainment of a lesser value of the Urbach energy for the TZNE glass (without NPs content) signified a material with a smaller impulse to convert weak bonds into defects [46]. The Urbach energy was increased with the addition of the TiO₂ and Al₂O₃ NPs, indicating a rising degree of disorder in the glass [47]. The

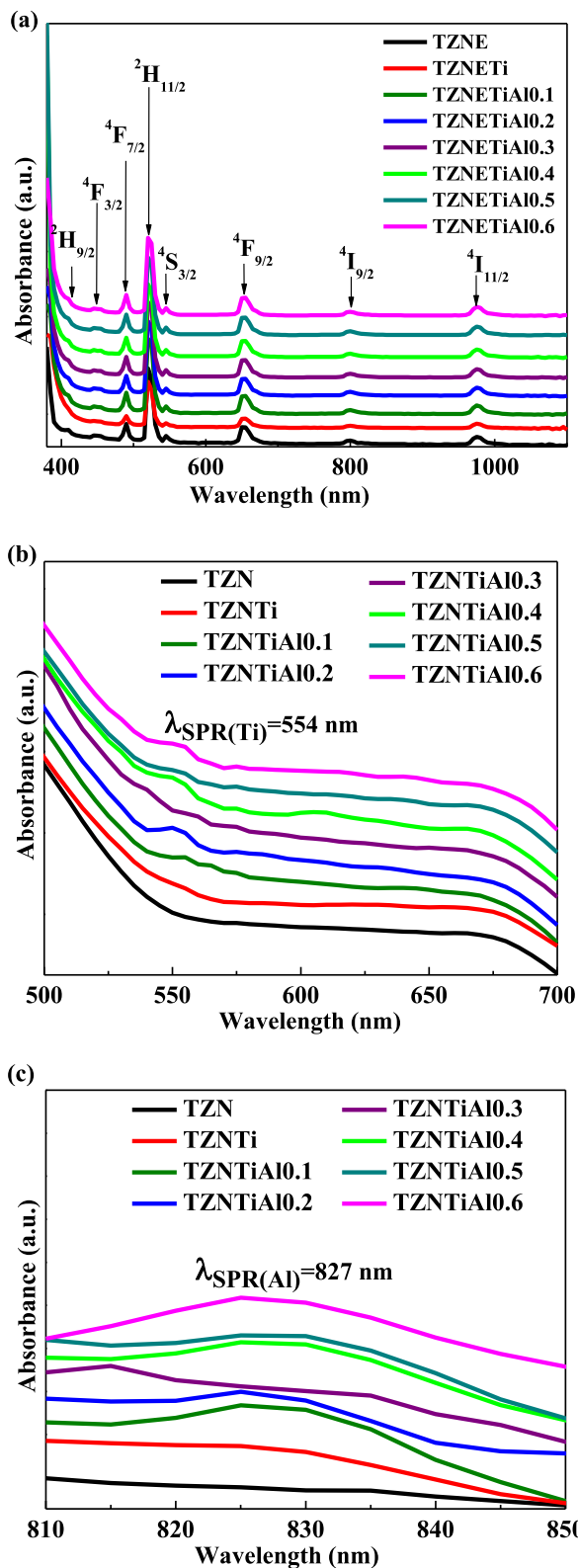


Fig. 8. Absorption spectra of prepared glass (a) with erbium content and (b) without erbium content in the range of 500 nm–700 nm to locate the Ti band position (c) without erbium content in the range of 810 nm–850 nm to locate the Al band position.

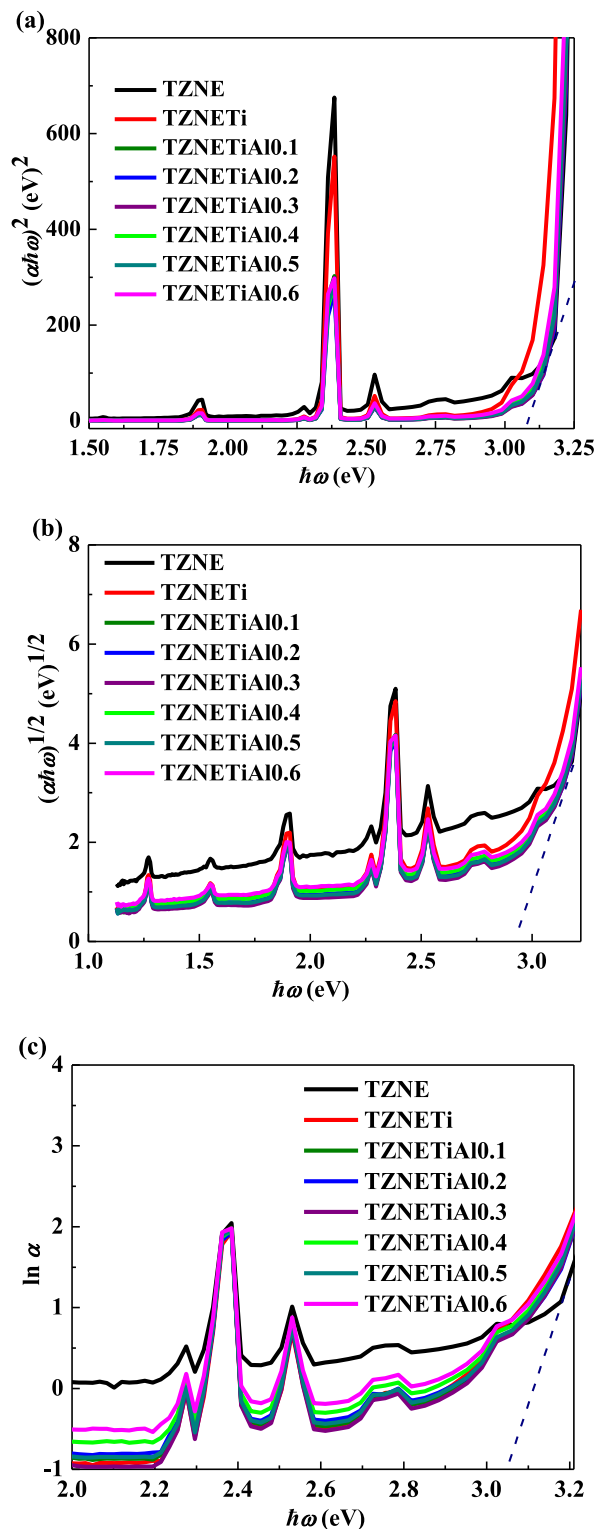


Fig. 9. (a) Tauc plot for direct band gap (b) Tauc plot for indirect band gap (c) Plot of $\ln \alpha$ versus photon energy.

observed behaviors clearly disclosed the expansion of the localized states within the gap [48]. Table 3 illustrates the variation in the direct band gap, indirect band gap, and Urbach energy of the glass samples with varying concentration of NPs.

Fig. 10a exemplifies the excitation spectra of glass containing varying concentrations of TiO_2 and Al_2O_3 . Eleven transitions in the Er^{3+} such as $^4I_{15/2} \rightarrow ^6D_{8/2}$, $^4I_{15/2} \rightarrow ^6D_{7/2}$, $^4I_{15/2} \rightarrow (^2D, ^2P, ^2F)_{3/2}$, $^4I_{15/2} \rightarrow ^2G_{7/2}$,

Table 3
Variation in the E_{dir} , E_{indir} , and E_U of prepared glass.

Glass code	E_{dir} (eV)	E_{indir} (eV)	E_U (eV)
TZNE	3.161	3.063	0.232
TZNETi	3.146	2.920	0.329
TZNETiAl0.1	3.165	3.104	0.376
TZNETiAl0.2	3.163	3.104	0.399
TZNETiAl0.3	3.161	3.100	0.369
TZNETiAl0.4	3.161	3.098	0.414
TZNETiAl0.5	3.160	3.098	0.387
TZNETiAl0.6	3.160	3.091	0.428

Table 4
Variation in the surface plasmon bands and PL maximum enhancement factor of glass with varying TiO₂ and Al₂O₃ contents.

Glass code	$\lambda_{SPR(Ti)}$ (nm)	$\lambda_{SPR(Al)}$ (nm)	Glass code	$\eta_{max(PL)}$ 547:668
TZN	–	–	TZNE	1:1
TZNETi	554	–	TZNETi	4.59 : 8.37
TZNETiAl0.1	554	827	TZNETiAl0.1	2.31 : 1.86
TZNETiAl0.2	554	827	TZNETiAl0.2	3.09 : 3.02
TZNETiAl0.3	554	827	TZNETiAl0.3	2.70 : 2.14
TZNETiAl0.4	554	827	TZNETiAl0.4	3.52 : 3.27
TZNETiAl0.5	554	827	TZNETiAl0.5	3.78 : 2.81
TZNETiAl0.6	554	827	TZNETiAl0.6	3.54 : 2.55

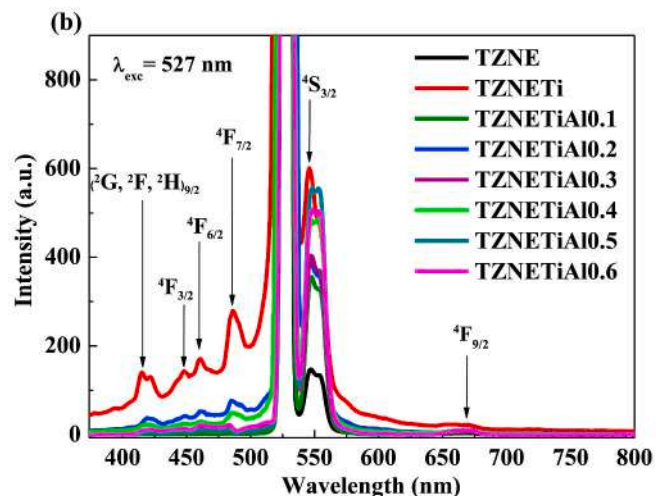
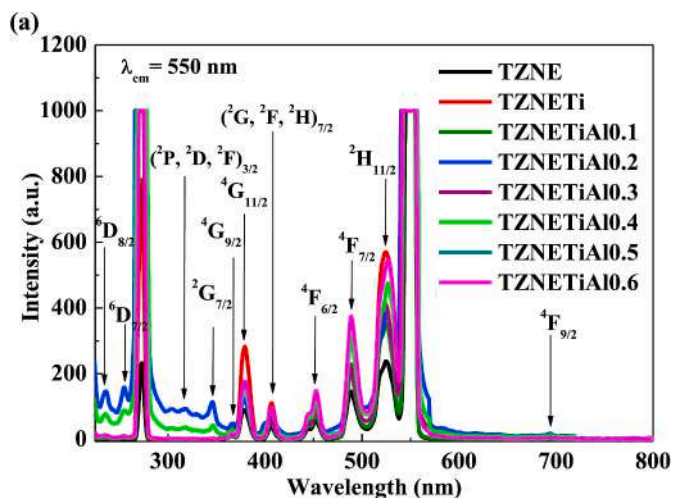


Fig. 10. (a) Excitation spectra of glass with emission wavelength of 550 nm (b) Emission spectra of glass with excitation wavelength of 527 nm.

$^4I_{15/2} \rightarrow ^4G_{9/2}$, $^4I_{15/2} \rightarrow ^4G_{11/2}$, $^4I_{15/2} \rightarrow (^2G, ^2F, ^2H)_{7/2}$, $^4I_{15/2} \rightarrow ^4F_{6/2}$, $^4I_{15/2} \rightarrow ^4F_{7/2}$, $^4I_{15/2} \rightarrow ^2H_{11/2}$, and $^4I_{15/2} \rightarrow ^4F_{9/2}$ produced the corresponding characteristics bands positioned at 235 nm, 254 nm, 317 nm, 347 nm, 365 nm, 379 nm, 406 nm, 452 nm, 488 nm, 527 nm, and 695 nm, respectively. The most prominent band positioned at 527 nm was used as the excitation wavelength to probe the emission spectra.

Fig. 10b shows the emission spectra of glass without and with TiO₂ and Al₂O₃ NPs. The emission spectra disclosed six characteristic bands of Er³⁺ centered at 415 nm, 447 nm, 459 nm, 486 nm, 547 nm, and 668 nm arising from $(^2G, ^2F, ^2H) \rightarrow ^4I_{15/2}$, $^4F_{3/2} \rightarrow ^4I_{15/2}$, $^4F_{6/2} \rightarrow ^4I_{15/2}$, $^4F_{7/2} \rightarrow ^4I_{15/2}$, $^4S_{3/2} \rightarrow ^4I_{15/2}$, and $^4F_{9/2} \rightarrow ^4I_{15/2}$ transitions, respectively. Four

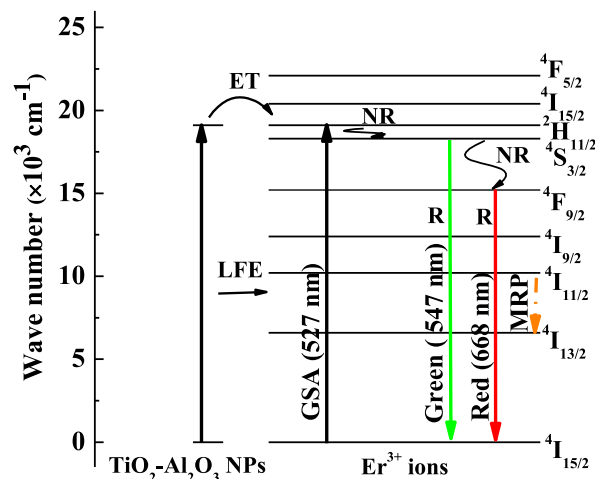


Fig. 11. Mechanism involved in the generation of emission spectra.

bands in the blue region (at 415 nm, 447 nm, 459 nm, and 486 nm) were excluded due to unfavorable bright blue emissions involving the pumping process of the three-step energy transfer [49]. The maximum enhancement factor of emission spectra was determined using $\eta_{max} = I_{sample(n)}/I_{reference}$ where $I_{sample(n)}$ represents the intensity of the TZNETi, TZNETiAl0.1, TZNETiAl0.2, TZNETiAl0.3, TZNETiAl0.4, TZNETiAl0.5, and TZNETiAl0.6 glass samples, and $I_{reference}$ denoted the intensity of the TZNE glass sample.

A comparison among the emission spectra revealed that the transition of the glass containing the monometallic TiO₂ NPs (TZNETi glass) was greatly enhanced for the band positioned at 668 nm corresponding to the $^4F_{9/2} \rightarrow ^4I_{15/2}$ transition (red band) with an enhancement factor of 8.37. The incorporation of the Al₂O₃ content showed a drastic change in the emission spectra of the glasses containing bimetallic NPs (TZNETiAl0.1, TZNETiAl0.2, TZNETiAl0.3, TZNETiAl0.4, TZNETiAl0.5, and TZNETiAl0.6 glass). An apparent enhancement was observed for the band positioned at 547 nm corresponding to $^4S_{3/2} \rightarrow ^4I_{15/2}$ transition (green band) with an enhancement factor of 3.78. The noticeable enhancement in different regions was observed due to the main contribution of the Ti plasmon band ($\lambda_{SPR(Ti)} = 554$ nm). According to Singh et al. [50], Er³⁺ exhibits small absorption cross-section. Thus, an alteration in their free space spectral properties and improvement in the yield of their weak optical transition can be attained through the incorporation of the conducting NPs in the vicinity of Er³⁺ [51]. In the present study, the incorporation of TiO₂ NPs stimulated the amplification of the local fields with energy transfer from TiO₂ NPs to Er³⁺. During the interaction, the TiO₂ NPs became the focal point of energy direction when NPs were stimulated with plasmon frequency and subsequently induced a prominent field enhancement in the vicinity of TiO₂ NPs [52]. Therefore, an intensification of electromagnetic fields around the Er³⁺ due to the SPR excitation led to the enhancement in the luminescence intensity of Er³⁺ ions [53]. However, attenuation in the PL

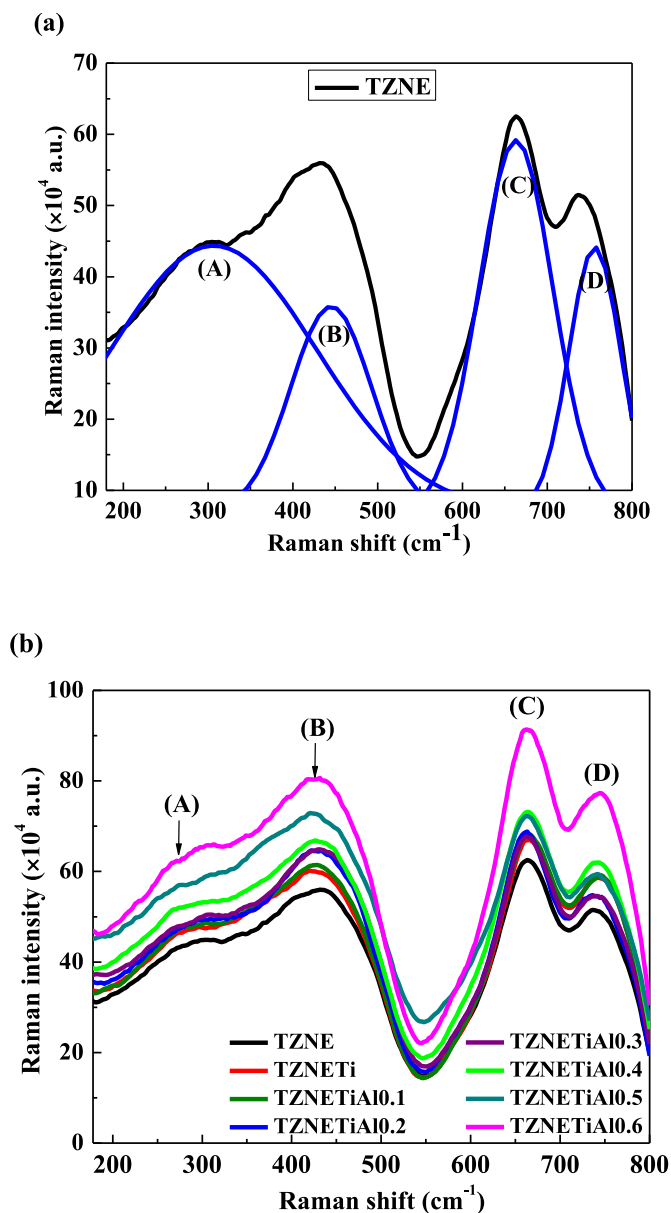


Fig. 12. Raman spectra of (a) glass without NPs and de-convolution into Gaussian peaks and (b) prepared glass with varying NPs content.

Table 5
Spectral region, Raman band assignments, and bonding vibrations.

Spectral region	Raman band (cm^{-1})	Characteristic structural elements
A	278	TeO ₃ tp bonds and Er-O bonds
B	427	Formation of Al-O-Al and Te-O-Al bonds
C	662	Te _{-eq} O _{ax} -Te bonds
D	744	TeO ₃ and TeO ₃₊₁ subunits

intensity was evidenced by the addition of the Al₂O₃ content. The attenuation occurred due to the properties of Al³⁺ that is non luminous [54] and generates disorder to the local environment around the Er³⁺, which leads to the attenuation in PL intensity [55]. According to Ikeda et al. [56], OH groups present on Al₂O₃ affect the photoluminescence emission of the glass. Therefore, addition of higher Al₂O₃ content in TZNETiAl0.6 glass shows an apparent reduction in the emission spectra for the band position at 547 nm due to the increasing OH hydroxyl groups, which is well-known as serious quenchers of Er³⁺ ions

Table 6

Range of size of NPs, surface roughness, and enhancement factor of Raman spectra.

Glass code	Longitudinal size NPs, L (nm)	Transverse size NPs, D (nm)	Surface roughness, R _q (nm)	n _{max} (Raman) 278::427:662:744
TZNE	-	-	-	1 : 1 : 1 : 1
TZNETi	15–34	11–20	6.1	1.05 : 1.04 : 1.06 : 1.02
TZNETiAl0.1	-	-	-	1.03 : 1.07 : 1.07 : 1.10
TZNETiAl0.2	-	-	-	1.10 : 1.11 : 1.10 : 1.12
TZNETiAl0.3	26–39	19–35	-	1.11 : 1.13 : 1.11 : 1.19
TZNETiAl0.4	-	-	-	1.34 : 1.14 : 1.20 : 1.28
TZNETiAl0.5	-	-	-	1.51 : 1.30 : 1.29 : 1.33
TZNETiAl0.6	25–48	19–32	9.3	1.55 : 1.45 : 1.51 : 1.61

luminescence [57]. Further details of maximum enhancement factor (n_{max}) in the Er³⁺ fluorescence of the prepared glasses are summarized in Table 4.

Fig. 11 illustrates the partial energy level diagram of Er³⁺ implying a few important steps that produced the emission spectra of the glasses containing varying concentrations of TiO₂ and Al₂O₃ NPs. The occurrence of PL emission at 547 nm and 668 nm was facilitated by the ground state absorption (GSA). It was followed by the energy transfer (ET) between the TiO₂-Al₂O₃ NPs and erbium ions. In addition, the local field effect was stimulated by the presence of TiO₂-Al₂O₃ NPs. The radiative decay (R) and non-radiative decay (NR) occurred during the optical interaction between the constituent atoms. A specific mechanisms occurred during the optical interaction can be explained as follows: (1) the excitation of Er³⁺ ions to ²H_{11/2} excited states stimulated by the laser beam of 527 nm wavelength, (2) the population of ⁴I_{11/2} and ⁴I_{13/2} excited states through a fast NR decay via multi-phonon relaxation process, (3) the NR decays from ²H_{11/2} to ⁴S_{3/2} populate this level and generate the green emission, (4) the red emission was favored by the NR decays from ⁴S_{3/2} to ⁴F_{9/2} populate the later level. The present findings are in good agreement with those previously reported by Sahar et al. [58] and Venkatramu et al. [59].

Fig. 12 illustrates the Raman spectra of the prepared glass samples. Fig. 12a shows the Raman spectra de-convoluted into four Gaussian peaks for TZNE glass. The observed four peaks centered at 278 cm^{-1} (A), 427 cm^{-1} (B), 662 cm^{-1} (C), and 744 cm^{-1} (D) corresponding to the bonding formation in the glass matrix. The appearance of peaks at lower frequency of 278 cm^{-1} represented the TeO₃ tp and Er-O bond [60–62]. The incorporation of the Er₂O₃ content in the glass matrix generated a structural modification, leading to the variation in the energy location of the Boson band [63]. Meanwhile, the occurrence of the peaks positioned at 427 cm^{-1} indicated the metal bond vibrations induced by the Al-O-Al and Te-O-Al bonds [64]. The observed peaks at around 662 cm^{-1} was due to the Te_{-eq}O_{ax}-Te bonds anti-symmetric vibrations that exhibited the long and short Te-O bonds [65–67]. The peaks at 744 cm^{-1} corresponding to the TeO₃₊₁ units represented the symmetric stretching vibrations between Te and non-bridging oxygen (NBO). This peak also signified the stretching mode of TeO₃ unit [47]. Further details on the spectral region, Raman band assignments, and bonding vibrations are summarized in Table 5.

Fig. 12b demonstrates the Raman spectra of the glass samples with varying TiO₂ and Al₂O₃ contents. The enhancement in the Raman intensity was obtained by dividing the intensity of glass samples containing NPs (TZNETi, TZNETiAl0.1, TZNETiAl0.2, TZNETiAl0.3, TZNETiAl0.4, TZNETiAl0.5, and TZNETiAl0.6 glass) to the reference glass sample without NPs (TZNE glass). The observed four peaks in TZNETiAl0.6 glass displayed the maximum enhancement factor of 1.55,

1.45, 1.51, and 1.61. The observed intensification in the Raman signal was attained with the increase in the Al_2O_3 concentration [60]. The current findings are in good agreement with previous studies conducted by Chao et al. [68], where the Raman enhancement factor was observed within the range of two orders of magnitude. The intensification in the Raman signal occurred due to the electromagnetic effect signifying the potential in the SERS activity [1] triggered by the excitation of the surface plasmon originated from the metal nanostructures [3]. In this case, bimetallic TiO_2 and Al_2O_3 nanoparticles act as mediators in the glass matrix [69]. The occurrence of significant polarization of molecules originates from the prominent electric field intensity when a Raman scattering molecule experiences strong electromagnetic fields generated on the metal surfaces and consequently causes an eminent induced dipole moment [1]. In addition, the intensification in Raman signal is assisted by the molecules existing in close vicinity to a rough noble metal surface [3]. Roughening at the surface of metals increases the surface area for interaction between the electromagnetic field and metals and subsequently leads to the amplification in Raman signal [4].

The highest Raman signal amplification was obtained for the TZNETiAl0.6 glass with surface roughness (R_q) of 9.3 nm and NPs with the size of 25–48 nm along the longitudinal axis. Our findings are in close agreement with those of Liu et al. [70] and Wijesuriya et al. [71] in which the amplification of Raman signal is triggered by an increase in the surface roughness and growth of metal NPs. La Porta et al. [72] reported that the diameter and shape of NPs affect the SERS enhancement. In the present study, significant enhancement in the Raman signal is achieved by free electrons on anisotropic nanoparticles generate a strong surface electric field upon electromagnetic excitation [51]. According to Xu et al. [69], the extensive curved or the existence of gap in metal region with substantial incident light conditions stimulates a giant enhancement in the local electromagnetic fields, which is known as a hot spot through localized surface plasmon resonance effect and causes the enhancement in the Raman signal. The size of NPs, surface roughness, and the enhancement factor of Raman spectra are tabulated in Table 6.

4. Conclusion

The TiO_2 and Al_2O_3 bimetallic NPs contents in the Er^{3+} tellurite glass were manipulated in this study for the first time to modify their surface topography, structural, and optical properties useful for the SERS applications. The TEM images of the glass samples showed the successful nucleation of both NPs in the host matrix where the lattice fringes revealed the lattice spacing of 3.78 Å and 4.79 Å for the TiO_2 and Al_2O_3 NPs, respectively. The formation of individually-scattered and wide islands was evidenced in the AFM images. The SPR bands of NPs were probed at 554 nm and 827 nm. The incorporation of TiO_2 NPs in the TZNETi glass enhances the emission intensity by a factor of 4.59 and 8.37 for ${}^2\text{H}_{11/2} \rightarrow {}^4\text{I}_{15/2}$ and ${}^4\text{F}_{9/2} \rightarrow {}^4\text{I}_{15/2}$ transitions. Meanwhile, the enhancement in the emission intensity of TZNETiAl0.5 glass in ratio of 3.78 and 2.81 due to the contribution of $\text{TiO}_2/\text{Al}_2\text{O}_3$ NPs. A significant enhancement in the luminescence intensity was achieved due to the interactions between the coupled metallic NPs and Er^{3+} with the excitation beams. Modification in the size and shape of NPs was responsible for the substantial enhancement in the Raman signal driven by the intense electric field of the bimetallic TiO_2 and Al_2O_3 NPs. The present strategy is established to be advantageous for altering the surface topography, size, and shape distribution of NPs where a careful control of the bimetallic NPs concentration may contribute to the development of new types of glass-based SERS substrates.

Author statement

Ixora Ferodolin: Data curation, Writing – original draft. Asmahani Awang: Conceptualization, Writing – review & editing, Project administration. S.K. Ghoshal: Writing – review & editing. Alireza Samavati: Writing – review & editing. Chee Fuei Pien: Data curation. Jedol Dayou:

Data curation.

Declaration of competing interest

The authors declare that they have no known competing financial interests or personal relationships that could have appeared to influence the work reported in this paper.

Acknowledgements

The authors are thankful to the Ministry of Higher Education Malaysia (MoHE), Universiti Malaysia Sabah and Universiti Teknologi Malaysia for the financial support under the Fundamental Research Grant Scheme (vote FRG0507-1/2019 & 5F050), Innovation Grant Scheme (vote SGI0053-2018), UMSGreat (vote GUG0200-1/2018) and UTMFR 20H65.

References

- [1] M. Kahraman, E.R. Mullen, A. Korkmaz, S. Wachsmann-Hogiu, Fundamentals and applications of SERS-based bioanalytical sensing, *J. Nanophotonics* 6 (2017) 831–852.
- [2] J.B. Jackson, N.J. Halas, Surface-enhanced Raman scattering on tunable plasmonic nanoparticle substrate, *Proc. Natl. Acad. Sci. Unit. States Am.* 101 (2004) 17930–17935.
- [3] S. Okeil, J.J. Schneider, Controlling surface morphology and sensitivity of granular and porous silver films for surface-enhanced Raman scattering, *SERS, Beilstein J. Nanotechnol.* 9 (2018) 2813–2831.
- [4] M. Fan, G.F.S. Andrade, A.G. Brolo, A review on the fabrication of substrates for surface enhanced Raman spectroscopy and their applications in analytical chemistry, *Anal. Chim. Acta* 693 (2011) 7–25.
- [5] P. Suchomel, R. Prucek, K. Cerna, A. Fargasova, A. Panacek, A. Gedanken, R. Zboril, L. Kvitek, Highly efficient silver particle layers on glass substrate synthesized by the sonochemical method for surface enhanced Raman spectroscopy purposes, *Ultrason. Sonochem.* 32 (2016) 165–172.
- [6] J. Deng, J. Dong, P. Cohen, Rapid fabrication and characterization of SERS substrates, *Procedia Manufacturing* 26 (2018) 580–586.
- [7] T. Wang, J. Zhou, Y. Wang, Simple, low-cost fabrication of highly uniform and reproducible SERS substrates composed of Ag-Pt nanoparticles, *Nanomaterials* 8 (2018) 331.
- [8] F. Guo, H. Yang, J. Mao, J. Huang, X. Wang, Y. Lai, Bioinspired fabrication SERS substrate based on superwetttable patterned platform or multiphase high-sensitive detecting, *Compos. Commun.* 10 (2018) 151–156.
- [9] S.A. Razek, A.B. Ayoub, M.A. Swillam, One step fabrication of highly absorptive and surface enhanced Raman scattering (SERS) silver nano-trees on silicon substrate, *Sci. Rep.* 9 (2019) 13588.
- [10] F. Chu, S. Yan, J. Zheng, L. Zhang, H. Zhang, K. Yu, X. Sun, A. Liu, Y. Huang, A simple laser ablation-assisted method for fabrication of superhydrophobic SERS substrate on teflon film, *Nanoscale Res. Lett.* 13 (2018) 244.
- [11] V.V. Strelchuk, O.F. Kolomyts, E.B. Kaganovich, I.M. Krishchenko, B.O. Golichenko, M.I. Boyko, S.O. Kravchenko, I.V. Kruglenko, O.S. Lytvyn, E.G. Manoilov, I. M. Nasieka, Optical characterization of SERS substrates based on porous Au films prepared by pulsed laser deposition, *J. Nanomater.* 203515 (2015) 1–7.
- [12] S.J. Henley, S.R. P. Silva, Laser direct write of silver nanoparticles from solution onto glass substrates for surface-enhanced Raman spectroscopy, *Appl. Phys. Lett.* 91 (2007), 023107.
- [13] M. Culha, B. Cullum, N. Lavrik, C.K. Klutse, Surface-enhanced Raman scattering as an emerging characterization and detection technique, *J. Nanotechnol.* 971380 (2012) 1–15.
- [14] A. Trugler, J.-C. Tinguely, G. Jakopic, U. Hohenester, J.R. Krenn, A. Hohenau, Near-field and SERS enhancement from rough plasmonic nanoparticles, *Phys. Rev. B* 89 (2014) 165409.
- [15] U.O.A. Arier, F.Z. Tepehan, Influence on $\text{Al}_2\text{O}_3/\text{TiO}_2$ ratio on the structural and optical properties of $\text{TiO}_2\text{-Al}_2\text{O}_3$ nano-composite films produced by sol gel method, *Composites Part B* 58 (2014) 147–151.
- [16] C. Demirbas, A. Ayday, The influence of nano- TiO_2 and nano- Al_2O_3 particles in silicate based electrolytes on microstructure and mechanical properties of micro arc Ti6Al4V alloy, *Mat. Res.* 21 (2018) 1–5.
- [17] D.M. Chien, N.N. Viet, N.T.K. Van, N.T.P. Phong, Characteristics modification of TiO_2 thin films by doping with silica and alumina for self-cleaning application, *J. Exp. Nanosci.* 4 (2009) 221–232.
- [18] S.-Z. Chu, S. Inoue, K. Wada, D. Li, H. Haneda, Highly porous $\text{TiO}_2/\text{Al}_2\text{O}_3$ composite nanostructures on glass by anodization and the sol-gel process: fabrication and photocatalytic characteristics, *J. Mat. Chem.* 13 (2003) 866–870.
- [19] E. Gjorgievska, J.W. Nicholson, D. Gabric, Z.A. Guclu, I. Miletic, N.J. Coleman, Assessment of the impact of the addition of nanoparticles on the properties of glass-ionomer cements, *Materials* 13 (2020) 276.
- [20] M.R. Khademolhosseini, M.H. Barounian, A. Eskandari, M. Aminzare, A.M. Zahedi, D. Ghahremani, Development of new $\text{Al}_2\text{O}_3/\text{TiO}_2$ reinforced glass-ionomer cements (GICs) nano-composites, *J. Basic Appl. Sci. Res.* 2 (2012) 7526–7529.

- [21] V. Piriawong, V. Thongpool, P. Asanithi, P. Limsuwan, Preparation and characterization of alumina nanoparticles in deionized water using laser ablation technique, *J. Nanomater.* 819403 (2012) 1–6.
- [22] M. Riazian, Nanostructural characterization and lattice strain of $\text{TiO}_2\text{-Al}_2\text{O}_3\text{-SiO}_2$ coating on glass and Si (100) substrates, *J. Chil. Chem. Soc.* 61 (2016) 2870–2877.
- [23] M. Gallart, T. Cottineau, B. Honerlage, V. Keller, N. Keller, P. Gilliot, Temperature dependent photoluminescence of anatase and rutile TiO_2 single crystals: polaron and self-trapped exciton formation, *J. Appl. Phys.* 124 (2018) 133104.
- [24] F.M. Fudzi, H.M. Kamari, A.A. Latif, A.M. Noorazlan, Linear optical properties of zinc borotellurite glass doped with lanthanum oxide nanoparticles for optoelectronic and photonic application, *J. Nanomater.* 2017 (2017) 1–8.
- [25] C.R. Giles, E. Desurvire, Moeling erbium-doped fiber amplifiers, *J. Lightwave Technol.* 9 (1991) 271–283.
- [26] R. El-Mallawany, M.D. Abdalla, A. Ahmed, New tellurite glass: optical properties, *J. Mat. Chem. Phys.* 109 (2008) 291–296.
- [27] P.S. Prasad, P.V. Rao, Structural and luminescence properties of tellurite glasses for laser applications, in: *Tellurite Glass Smart Materials*, Springer, Cham, 2018.
- [28] Y. Qi, Y. Zhou, L. Wu, F. Yang, S. Peng, S. Zheng, D. Yin, Silver nanoparticles enhanced 1.53 μm band fluorescence of $\text{Er}^{3+}/\text{Yb}^{3+}$ co-doped tellurite glasses, *J. Lumin.* 153 (2014) 401–407.
- [29] K. Selvaraju, K. Marimuthu, Structural and spectroscopic studies on concentration dependent Sm^{3+} doped bororo-tellurite glasses, *J. Alloys Compd.* 553 (2013) 273–281.
- [30] S.H. Alazoumi, S.A. Aziz, R. El-Mallawany, U.S. Aliyu, H.M. Kamari, M.H.M. Zaid, K.M. Matori, A. Ushah, Optical properties of zinc lead tellurite glasses, *Results in Phys* 9 (2018) 1371–1376.
- [31] R.P.V. Duyne, J.C. Hulst, D.A. Treichel, Atomic force microscopy and surface-enhanced Raman spectroscopy. I. Ag island films and Ag film over polymer nanosphere surfaces supported on glass, *J. Chem. Phys.* 99 (1993) 2101–2115.
- [32] G. Seifert, A. Stalmashonak, H. Hofmeister, J. Haug, M. Dubiel, Laser-induced, polarization dependent shape transformation of Au/Ag nanoparticles in glass, *Nanoscale Res. Lett.* 4 (2009) 1380–1383.
- [33] G. Paramasivam, N. Kayambu, A.M. Rabel, A.K. Sundramoorthy, A. Sundaramurthy, Anisotropic noble metal nanoparticles: synthesis, surface functionalization and applications in biosensing, bioimaging, drug delivery and theranostics, *Acta Biomater.* 49 (2017) 45–65.
- [34] S. Chervinskii, R. Drevinskas, D.V. Karpov, M. Beresna, A.A. Lipovskii, Y.P. Svirko, P.G. Kazansky, Revealing the nanoparticles aspect ratio in the glass-metal nanocomposites irradiated with femtosecond laser, *Sci. Rep.* 5 (2015) 13746.
- [35] O. Avilés-García, J. Espino-Valencia, R. Romero-Romero, J.L. Rico-Cerda, M. Arroyo-Albiter, D.A. Solís-Casados, R. Natividad-Rangel, Enhanced photocatalytic activity of titania by co-doping with Mo and W, *Catalysts* 8 (2018) 631.
- [36] M. Riazian, Dependence of photocatalytic activity of $\text{TiO}_2\text{-SiO}_2$ Nanopowders, *J. Nanomater.* 4 (2014) 433–441.
- [37] H.-H. Kim, Y.-S. Lee, D.C. Chung, B.-J. Kim, Studies on preparation and characterization of aluminium nitride-coated carbon fibers and thermal conductivity of epoxy matrix composites, *Coatings* 7 (2017) 121.
- [38] H. Hofmeister, G.L. Tan, M. Dubiel, Shape and internal structure of silver nanoparticles embedded in glass, *J. Mat. Res.* 20 (2005) 1551–1562.
- [39] H. Fares, H. Elhouichet, B. Gelloz, M. Ferid, Surface plasmon resonance induced Er^{3+} photoluminescence enhancement in tellurite glass, *J. Appl. Phys.* 117 (2015) 193102.
- [40] S.R. Naidoo, A. Ismaila, Fluence enhanced optical response of Ag implanted amorphous carbon thin films, *J. Carbon Res.* 5 (2019) 1–12.
- [41] H. Kuzmany, *Solid State Spectroscopy*, second ed., Springer, New York, 2009.
- [42] M.K. Halimah, M.F. Faznny, M.N. Azlan, H.A.A. Sidek, Optical basicity and electronic polarizability of zinc borotellurite glass doped La^{3+} ions, *Results in Phys* 7 (2017) 581–589.
- [43] S. Rosmawati, H.A.A. Sidek, A.T. Zainal, H.M. Zobir, IR and UV spectral studies of zinc tellurite glasses, *J. Appl. Sci.* 7 (2007) 3051–3056.
- [44] X. Kang, S. Liu, Z. Dai, Y. He, X. Song, Z. Tan, Titanium dioxide: from engineering to applications, *Catalysts* 9 (2019) 191.
- [45] M.J. Akhtar, H.A. Alhadlaq, A. Alshamsan, M.A. Majeed Khan, M. Ahamed, Aluminum doping tunes band gap energy level as well as oxidative stress-mediated cytotoxicity of ZnO nanoparticles in MCF-7 cells, *Sci. Rep.* 5 (2015) 13876.
- [46] S.B. Kolavekar, N.H. Ayachit, G. Jagannath, K. NagaKrishnan, S.V. Rao, Optical, structural and near-IR NLO properties of gold nanoparticles doped sodium zinc borate glasses, *Opt. Mater.* 83 (2018) 34–42.
- [47] G. Upender, S. Ramesh, M. Prasad, V.G. Sathe, V.C. Mouli, Optical band gap, glass transition temperature and structural studies of $(100 - 2x)\text{TeO}_2\text{-xAg}_2\text{O-xWO}_3$ glass system, *J. Alloys Compd.* 504 (2010) 468–474.
- [48] M.K. Halimah, W.M. Daud, H.A.A. Sidek, A.W. Zaidan, A.S. Zainal, Optical properties of ternary tellurite glasses, *J. Mat. Sci. Pol.* 28 (2010) 173–180.
- [49] Y. Zhang, S. Xu, X. Li, J. Sun, J. Zhang, H. Zheng, H. Zhong, R. Hua, H. Xia, B. Chen, Concentration quenching of blue upconversion luminescence in $\text{Tm}^{3+}/\text{Yb}^{3+}$ co-doped $\text{Gd}_2(\text{WO}_4)_3$ phosphors under 980 and 808 nm excitation, *J. Alloys Compd.* 709 (2017) 147–157.
- [50] S.K. Singh, N.K. Giri, D.K. Rai, S.B. Rai, Enhanced upconversion emission in Er^{3+} -doped tellurite glass containing silver nanoparticles, *Solid State Sci.* 12 (2010) 1480–1483.
- [51] T. Som, B. Karmakar, Nanosilver enhanced upconversion fluorescence of erbium ions in Er^{3+} : Ag-antimony glass nanocomposites, *J. Appl. Phys.* 105 (2009), 013102.
- [52] S.A. Kalele, N.R. Tiwari, S.W. Gosavi, S.K. Kulkarni, Plasmon-assisted photonics at the nanoscale, *J. Nanophotonics* 1 (2007), 012501.
- [53] Z. Pan, A. Ueda, R. Aga Jr., A. Burger, R. Mu, S.H. Morgan, Spectroscopic studies of Er^{3+} doped Ge-Ga-S glass containing silver nanoparticles, *J. Non-Cryst. Solids* 356 (2010) 1097–1101.
- [54] P.A. Prashanth, R.S. Raveendra, R.H. Krishna, S. Ananda, N.P. Bhagya, B. M. Nagabhushana, K. Lingaraju, H.R. Naika, Synthesis, characterizations, antibacterial and photoluminescence studies of solution combustion-derived $\alpha\text{-Al}_2\text{O}_3$ nanoparticles, *J. Asian Ceram. Soc.* 3 (2015) 345–351.
- [55] K. Drdlikova, R. Klement, D. Drdlik, T. Spusta, D. Galusek, K. Maca, Luminescent Er^{3+} doped transparent alumina ceramics, *Analog Integr. Circuits Signal Process.* 37 (2017) 2695–2703.
- [56] H. Ikeda, T. Murata, S. Fujino, Fabrication and photoluminescence of monolithic silica glass doped with alumina nanoparticles using $\text{SiO}_2\text{-PVA}$ nanocomposite, *J. Ceram. Soc. Japan* 123 (2015) 550.
- [57] J. Massera, L. Petit, J. Koponen, B. Glorieux, L. Hupa, M. Hupa, $\text{Er}^{3+}\text{-Al}_2\text{O}_3$ nanoparticles doping of borosilicate glass, *Bull. Mater. Sci.* 38 (2015) 1407.
- [58] M.R. Sahar, S.K. Zain, N.A. Ishak, E.S. Szali, N.M. Yusoff, Physical and optical analysis of erbium doped magnesium zinc phosphate glass, *Res. Rev. J. Pure Appl. Phys.* 3 (2015) 18–23.
- [59] V. Venkatramu, S.F. Leon-Luis, U.R. Rodriguez-Mendoza, V. Monteseuro, F. J. Manjon, A.D. Lozano-Gorrin, R. Valiente, D. Navarro-Urrios, C.K. Jayasankar, A. Munoz, V. Lavin, Synthesis, structure and luminescence of Er^{3+} -doped $\text{Y}_3\text{Ga}_5\text{O}_{12}$ nano-garnets, *J. Mat. Chem.* 22 (2012) 13788–13799.
- [60] M.R. Dousti, M.R. Sahar, R.J. Amjad, S.K. Ghoshal, A. Awang, Surface enhanced Raman scattering and up-conversion emission by silver nanoparticles in erbium-zinc-tellurite glass, *J. Lumin.* 143 (2013) 368–373.
- [61] C. Gautam, A.K. Yadav, V.K. Mishra, K. Vikram, Synthesis, IR and Raman spectroscopic studies of (Ba, Sr) TiO_3 borosilicate glasses with addition of La_2O_3 , *J. Inorganic Non-Metal. Mat.* 2 (2012) 47–54.
- [62] T. Komatsu, H. Tawarayama, H. Mohri, K. Matsuta, Properties and crystallization behaviors of $\text{TeO}_2\text{-LiNbO}_3$ glasses, *J. Non-Cryst. Solids* 135 (1991) 105–113.
- [63] K. Venkatarao, M. Seshadri, C. Venkateswarlu, Y.C. Ratnakaram, Spectroscopic properties and Judd-Ofelt analysis of Sm^{3+} and Dy^{3+} doped chlorophosphate glasses, *IOP Conf. Ser. Mater. Sci. Eng.* 2 (2009), 012045.
- [64] A. Kaur, A. Khanna, M. González-Barriuso, F. González, B. Chen, Short-range structure and thermal properties of alumino-tellurite glasses, *J. Non-Cryst. Solids* 470 (2017) 14–18.
- [65] O. Noguera, T. Merle-Mejean, A.P. Mirgorodsky, M.B. Smirnov, P. Thomas, J. C. Champarnaud-Mesjard, Vibrational and structural properties of glass and crystalline phases of TeO_2 , *J. Non-Cryst. Solids* 330 (2004) 50–60.
- [66] T. Sekiya, N. Mochida, A. Ohtsuka, Raman spectra of MO-TeO_2 ($M = \text{Mg, Sr, Ba}$ and Zn) glasses, *J. Non-Cryst. Solids* 168 (1994) 106–114.
- [67] G.S. Murugan, Y. Ohishi, Raman spectroscopic studies of $\text{TeO}_2\text{-BaO-SrO-Nb}_2\text{O}_5$ glasses: structure-property correlations, *J. Appl. Phys.* 96 (2004) 2437.
- [68] B.-K. Chao, Y. Xu, H.-C. Ho, P. Yiu, Y.-C. Lai, C.-H. Shek, C.-H. Hsueh, Gold-rich ligament nanostructure by dealloying Au-based metallic glass ribbon for surface-enhanced Raman scattering, *Sci. Rep.* 7 (2017) 7485.
- [69] W. Xu, X. Ling, J. Xiao, M.S. Dresselhaus, J. Kong, H. Xu, Z. Liu, J. Zhang, Surface enhanced Raman spectroscopy on a flat graphene surface, *Proc. Natl. Acad. Sci. Unit. States Am.* 109 (2012) 9281–9286.
- [70] Y.-C. Liu, P.-I. Lin, Y.-T. Chen, M.-D. Ger, K.-L. Lan, C.-L. Lin, Effect of TiO_2 nanoparticles on the improved surface-enhanced Raman scattering of polypyrrole deposited on roughened gold substrates, *J. Phys. Chem. B* 108 (2004) 14897–14900.
- [71] S. Wijesuriya, K. Burugapalli, R. Mackay, G.C. Ajaezi, W. Balachandran, Chemically roughened solid silver: a simple, robust and broadband SERS substrate, *Sensors* 16 (2016) 1742.
- [72] A. La Porta, M. Grzelczak, L.L. Liz-Marzan, Gold nanowire forests for SERS detection, *ChemistryOpen* 3 (2014) 146.